

Recent advances on hydrogen embrittlement of structural materials

Mohsen Dadfarnia · Akihide Nagao ·
Shuai Wang · May L. Martin ·
Brian P. Somerday · Petros Sofronis

Received: 11 November 2015 / Accepted: 15 December 2015 / Published online: 24 December 2015
© Springer Science+Business Media Dordrecht 2015

Abstract This paper presents a critical review of current understanding of the effect of hydrogen on fracture and fatigue of metals and alloys. First, microstructures found immediately beneath hydrogen-induced fracture surfaces in various materials are presented. Then, recent progress toward the fundamentals of hydrogen-induced fracture is reported. Lastly, a recent attempt to model hydrogen embrittlement by linking the macroscale (e.g. applied load and hydrogen content) and the operating microscopic degradation mechanism at the local microstructural defect level is reviewed.

Keywords Hydrogen embrittlement · Fracture · Fatigue · Plasticity · Dislocation · Microstructure

M. Dadfarnia · P. Sofronis (✉)
Department of Mechanical Science and Engineering,
University of Illinois at Urbana-Champaign, 1206 West
Green Street, Urbana, IL 61801, USA
e-mail: sofronis@illinois.edu

M. Dadfarnia
e-mail: dadfarni@illinois.edu

A. Nagao
Material Surface and Interface Science Research
Department, Steel Research Laboratory, JFE Steel
Corporation, Minamiwatarida-cho, Kawasaki-ku,
Kawasaki, Kanagawa 210-0855, Japan

S. Wang
Department of Materials Science and Engineering,
University of Wisconsin-Madison, 1415 Engineering Drive,
Madison, WI 53706, USA

1 Introduction

The degradation of the mechanical properties of materials by hydrogen, known as hydrogen embrittlement (HE), was first noted by Johnson more than a century ago when he studied the effect of the immersion in acids on the fracture properties of iron and steel (Johnson 1874). Since then, the hydrogen embrittlement phenomenon has been widely studied as demonstrated by many publications including several review articles addressing issues such as the role of microstructure on HE (Bernstein and Thompson 1984; Thompson and Bernstein 1980), mechanisms of HE (Birnbaum 1977; Birnbaum et al. 1997; Hirth 1984; Lynch 2011; Nagao et al. 2015),

M. L. Martin
Institut für Materialphysik, Georg-August-Universität
Göttingen, Friedrich-Hund-Platz 1, 37077 Göttingen, Germany

B. P. Somerday
Sandia National Laboratories, P.O. Box 969, Livermore,
CA 94551, USA

M. Dadfarnia · A. Nagao · S. Wang · B. P. Somerday ·
P. Sofronis
International Institute for Carbon-Neutral Energy Research
(WPI-I2CNER), Kyushu University, 744 Motooka,
Nishi-ku, Fukuoka, Fukuoka 819-0395, Japan

and the hydrogen effect on mechanical properties and fracture behavior (Hirth 1980; Moody et al. 1990; Robertson et al. 2009). The work is still being pursued today, driven by the need to find more compatible and economical materials for energy technology system applications (Gangloff and Somerday 2012; Somerday and Sofronis 2014).

Despite a century of work on this subject, the mechanism responsible for such premature failure is still being debated (Gerberich 2012; Robertson et al. 2015). Although many mechanisms have been proposed for explaining the degradation of materials in the presence of hydrogen, two mechanisms, hydrogen enhanced localized plasticity (HELP) (Beachem 1972; Birnbaum and Sofronis 1994) and hydrogen-induced decohesion (HID) (Gerberich et al. 1996; Oriani and Josephic 1977), are considered to be viable for structural materials that do not form hydrides. In the materials that can form hydrides because either they have stable hydrides or hydrides can be stabilized under applied stress (Flanagan et al. 1981), hydrogen embrittlement usually occurs through hydride formation and fracture (Shih et al. 1988; Takano and Suzuki 1974). Hydrogen-induced hydride formation is a well-accepted mechanism for materials such as Ti, Zr, Group Vb metals, and their alloys. As such, this mechanism is not considered in this paper. According to the HELP mechanism, hydrogen promotes macroscopic failures through localized shear and ductile rupture processes caused by enhancing the mobility of dislocations (Birnbaum 1977; Robertson 2001) via reducing the strength of barriers to dislocations motion (Sofronis and Birnbaum 1995). The HID mechanism states that hydrogen degrades the strength of materials by decreasing their cohesive energy along crystallographic planes or material interfaces (Geng et al. 1999; Van der Ven and Ceder 2004).

Besides reducing the fracture strength and work of fracture, hydrogen may also alter the fracture mode of structural materials. For example, for materials that are ductile involving void growth and coalescence in the absence of hydrogen, the fracture mode may be changed to transgranular “quasi-cleavage” fracture or even intergranular fracture in the presence of hydrogen. “Quasi-cleavage” is a fracture mode similar in appearance to cleavage in having planar facets but not along a known cleavage plane. A distinct feature of “quasi-cleavage” surfaces is the presence of fine ridges running mostly parallel to the crack propagation direction.

Although hydrogen-induced fracture surface morphology shows the degree of hydrogen embrittlement, it may not be accurate for gaining insight about the deformation process preceding the fracture.

Progress in developing experimental techniques has enabled researchers to better characterize and study the microstructure of materials. One such technique is utilizing focused-ion beam (FIB) machining to extract transmission electron microscopy (TEM) samples from site-specific locations on the surface of structural materials (Munroe 2009). The location, for example, can be on the specimen surface at or ahead of the crack tip to study the evolved microstructure of the material ahead of a crack, or on a fracture surface of a failed sample to gain insight on the relation between the features on the fracture surface and the microstructure beneath them. In addition, recent advances in thermal desorption analysis (TDA) and related analysis methods have contributed to a clearer understanding of hydrogen distribution in materials through measurement of hydrogen content and also through determination of hydrogen trapping sites and the binding energy of hydrogen to the corresponding traps. This advance includes a recently developed new TDA system that can take hydrogen desorption data from -200°C (Takai 2011; Abe et al. 2010, 2011).

In this paper, we review experimental studies of the effect of hydrogen on fracture and fatigue of structural materials in connection with the microstructure directly under the fracture surface. Specifically, the microstructure associated with the fracture of a line pipe steel, nickel, iron, and a tempered lath martensitic steel and the fatigue of 304 and 316 stainless steels is presented. The approach is different from other studies in which the fracture surface is only examined without considering the microstructure developed beneath the fracture surface. For cases in which failure occurs at grain boundaries, the microstructures consistently demonstrated synergistic action of HELP and HID and resulted in proposition of a new mechanism of hydrogen embrittlement, i.e. hydrogen-induced plasticity-mediated decohesion mechanism. The fatigue case involves a recent study to quantify the effect of residual gas impurity concentration on preventing the hydrogen acceleration of fatigue crack growth under different mechanical variables. Then, as recent progress toward fundamental understanding of hydrogen-induced fracture mechanics, three topics follow: first, we give an overview of the results of molecu-

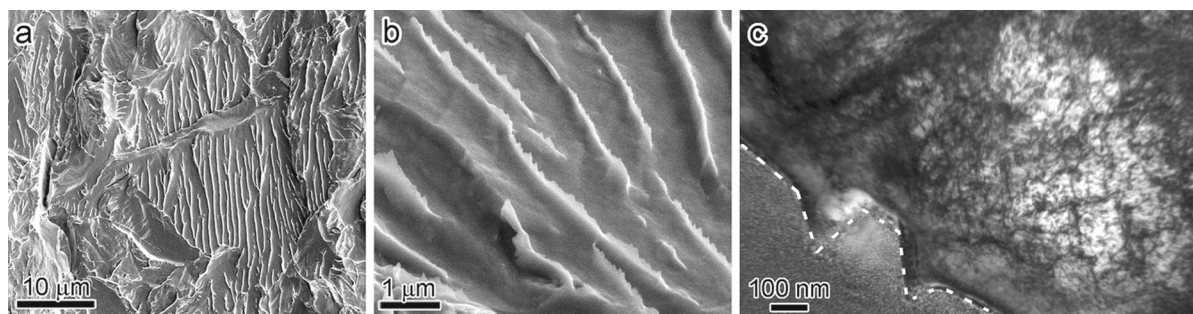


Fig. 1 Hydrogen-induced “quasi-cleavage” of an API X60 line pipe steel. **a** SEM micrograph of the fracture surface, **b** high magnification of the image, **c** TEM micrograph normal to the

“quasi-cleavage” fracture surface showing the microstructure underneath the surface. The fracture surface is shown by the dashed lines (Martin et al. 2011a)

lar statics calculations which shows that HID alone may not be enough to explain hydrogen-induced intergranular fracture. Second, a model is presented for hydrogen transport by mobile dislocation which can explain the evolved microstructures found far below hydrogen-induced fracture surfaces into the specimen. Third, recent progress in TDA that is a powerful tool for determining hydrogen distribution in materials is reviewed. Finally, we describe a statistically-based micromechanical model for prediction of the onset of crack initiation in a high-strength steel in the presence of hydrogen.

2 Hydrogen-induced transgranular fracture

Line pipe steels are usually medium or low strength ferritic steels which, due to their low cost and safety advantages, can be used for the distribution of hydrogen gas. Hydrogen embrittlement of the line pipe materials is one of the main problems in hydrogen distribution through pipeline networks. Hydrogen-induced fracture surface of line pipe steels has distinct morphologies including microvoid coalescence, secondary cracks, “flat” featureless regions and “quasi-cleavage” features. In the following, the study of the microstructures below the flat and “quasi-cleavage” regions in a line pipe steel is presented. The compact tension samples were made from an API X60 HIC grade line pipe steel and tested under slow rising load condition in high pressure hydrogen gas (21 MPa).

2.1 “Quasi-cleavage” surface of a line pipe steel

A feature that distinguishes “quasi-cleavage” from other fracture surfaces is parallel striations or river markings on “quasi-cleavage” fracture surfaces (Fig.

1a). Martin et al. (2011a) studied the “quasi-cleavage” fracture surface using high resolution SEM. As shown in Fig. 1b, there were thin electron transparent saw-teeth at the tip of most ridges. Comparing those saw-teeth features with ligaments formed in TEM foils strained to failure, they concluded that saw-teeth should be due to extensive plasticity during the final separation process of ridges and not essential to the hydrogen induced fracture of steel.

Using the FIB lift out technique, Martin et al. (2011a) extracted TEM samples under the “quasi-cleavage” regions. Figure 1c shows such a micrograph from a region normal to ridges with two closely spaced ridges on the fracture surface. Below ridges, slip bands are visible which are almost parallel to the ridge edges suggesting a fracture process governed by dislocation slip. Enhanced and confined slip activity under the fracture surface is consistent with the hydrogen enhanced localized plasticity mechanism and shielding model of hydrogen embrittlement (Robertson 2001).

The fact that no carbides were observed to be associated with the ridges showed that carbides do not have a role in the formation of these “quasi-cleavage” fracture surfaces. From studying the features on the “quasi-cleavage” surface and microstructure below that, Martin et al. (2011a) reasoned that the fracture process should involve void nucleation and growth at slip band intersections. They noted that voids nucleated at slip band intersections and along lines of the slip band intersections. Then each void expanded by dislocation processes until encountering another void and final failure took place along tops of ridges forming saw-teeth. The role of hydrogen was concluded to be the creation of a condition for development of dislocation structure such as slip bands and accelerating void initiation

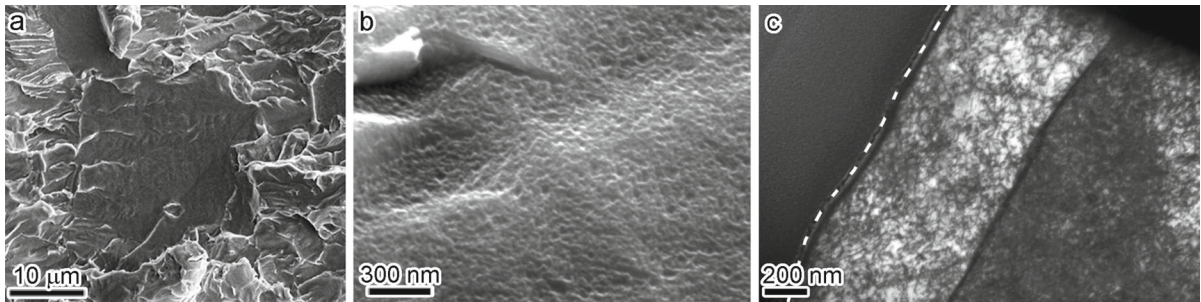


Fig. 2 “Flat” features (or featureless region) in hydrogen-induced fracture of an API X60 line pipe steel. **a** SEM micrograph of the fracture surface, **b** high resolution SEM micrograph, **c**

TEM micrograph showing the microstructure immediately under the flat surface illustrated by the *dashed line* (Martin et al. 2011b)

and growth through enhancing dislocation processes. Therefore, it was suggested that “quasi-cleavage” fracture surfaces are formed by hydrogen enhanced plasticity processes, not by a cleavage like process.

2.2 Flat surface morphology of a line pipe steel

Flat features or featureless regions which do not have any ridge are another surface morphology often observed on the hydrogen-induced fracture surfaces (Fig. 2a). These features were flat in plan-view, however, Martin et al. (2011b) examining the surfaces through high resolution SEM found out that what one sees as a flat surface in actuality is covered with undulations and rounded mounds as shown in Fig. 2b. The roughness of the featureless region was measured by atomic force microscopy (AFM) which revealed that the diameters of the mounds were about 50 nm and their height differences were about 5 nm. Looking at the microstructure beneath these surfaces, Martin et al. (2011b) observed a high density of dislocations which remained almost the same with no noticeable change over several microns under the fracture surface. Similar to the case of “quasi-cleavage” surface, it appeared that precipitates do not affect the crack path as some precipitates have been observed under the fracture surface with no influence on the fracture morphology.

Martin et al. (2011b) proposed that the plasticity and underlying dislocation structure plays a major role in establishing the conditions for the formation of surface morphology. Hydrogen, by promoting the condition for forming high dislocation density which increases the local hydrogen concentration, establishes weak regions for crack propagation. They proposed that the difference between the conditions which produce the “quasi-

cleavage” features (presented in Sect. 2.1) and the flat features (presented in this section) is the orientation and constraints on the grains leading to the development of different dislocation structures.

3 Hydrogen-induced intergranular fracture

Hydrogen changes the mode of fracture in some systems from ductile to brittle intergranular. This is more pronounced in high strength steels, and also under high hydrogen concentration conditions. The results of intergranular fracture of two different systems, namely face centered cubic (fcc) nickel and body centered cubic (bcc) iron, along with the study of the microstructures under their fracture surfaces are presented.

3.1 Intergranular fracture of Ni 201

Nickel exhibits a transition from a ductile failure mode with dimpled fracture surfaces to intergranular failure mode by increasing hydrogen concentration (Lassila and Birnbaum 1986) which is accompanied with a significant decrease in the strain to fracture. Martin et al. (2012) investigated the fracture surface of a commercially pure Ni (Ni-201 alloy) failed in the presence of hydrogen. The tensile specimen of Ni-201 alloy was precharged in hydrogen gas at elevated temperature to achieve a uniform lattice hydrogen concentration of about 2000 appm (Bechtle et al. 2009). The specimen was loaded at a constant strain rate of 4×10^{-4} /s until fracture. The hydrogen-charged specimen had 100 % intergranular fracture with strain to failure of 13 % which is significantly less than the 50–60 % strain to failure expected for uncharged Ni specimens.

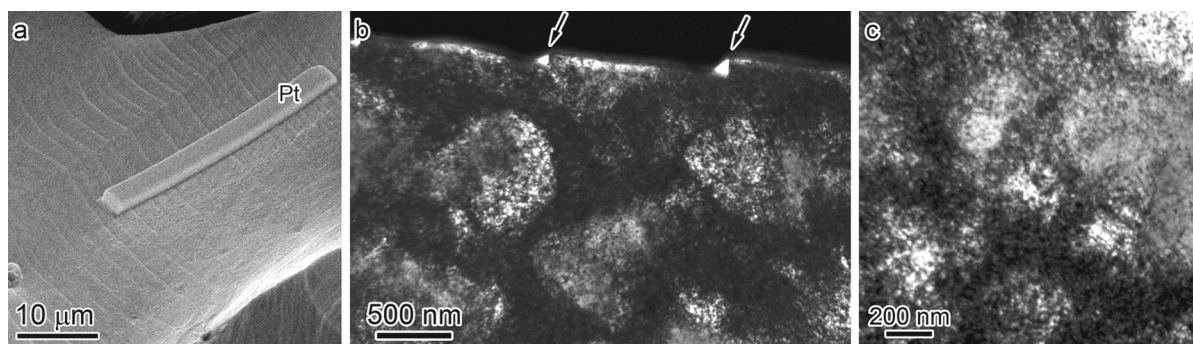


Fig. 3 Hydrogen-induced intergranular fracture of Ni 201, **a** micrograph showing the location of FIB lift out on the fracture surface, **b** TEM micrograph showing the microstructure immediately beneath the fracture surface, and **c** 4–5 μm below the fracture surface (Martin et al. 2012)

High-resolution SEM examination of the hydrogen-induced fracture surfaces revealed presence of slip lines on individual facets and some facets had evidence of more than one active slip system. Looking at the surface of facets with only one slip system traces on the surface, Fig. 3a, one may incorrectly interpret that only one slip system is active in the corresponding grain. Martin et al. (2012) extracted TEM samples normal to such fracture surfaces using FIB lift-out technique to understand the relation of the slip traces to the microstructure developed under the surface. As shown in Fig. 3b, dislocations in high densities existed under the fracture surface and multiple slip systems were active in the grain. Dislocations were organized into cell structures with average diameter of 200–400 nm. Even 4–5 μm away from the fracture surface the dislocation density was still high with almost the same cell size as the material immediately below the fracture surface as seen in Fig. 3c. This small dislocation structure change with depth is evidence that dislocations are not just ejected from the crack to the bulk. Even further from the fracture surface (~ 3 mm), the microstructure still consists of dislocation cells, though slightly larger, supporting the idea that the deformation is widespread and not limited to the crack tip region (Robertson et al. 2015). Based on the interpolation of the measured cell size as a function of strain from the work of Keller et al. (2010), it was found that in the absence of hydrogen a strain of 40 % is necessary to achieve 200–400 nm dislocation cell size. However, the macroscopic strain at failure was 13 % which suggests that a significant degree of refinement occurs in the presence of hydrogen.

diately beneath the fracture surface, and **c** 4–5 μm below the fracture surface (Martin et al. 2012)

Martin et al. (2012) argued that the formation of slip traces on the grain facets can be neither from emission of dislocations sources at or near a crack tip nor by near surface dislocations pulled to the surface by image forces. Rather, it should be associated with transmission of slip across the grain boundary before the failure. Presence of hydrogen on the grain boundary can reduce the cohesive energy of the grain boundary. Therefore, dislocations moving toward the grain boundary transport hydrogen with them and reduce the cohesive energy by increasing hydrogen concentration on the grain boundary. This is due to the fact that dislocation accommodation to the grain boundary and emission of new dislocations to the nearby grain is not usually one-to-one (Clark et al. 1992; Lee et al. 1990a, b). Moreover, accommodation and emission will increase the strain energy density and will further decrease the cohesive energy of the grain boundary. So it is proposed that hydrogen's role in intergranular fracture is twofold: raising the stress level by creating a complex microstructure and reducing the cohesive energy of the grain boundary. Therefore, it was concluded that hydrogen-induced plasticity plays an important role in establishing the local conditions for intergranular fracture.

In summary, hydrogen increases the density of dislocations and enhances their velocities. Due to this enhanced plasticity (HELP), more hydrogen carried by dislocations is deposited on the grain boundaries; the additional hydrogen accumulation further reduces the grain boundary cohesion. A combination of this reduction in the grain boundary cohesion and the locally enhanced stresses due to local strain hardening can result in decohesion.

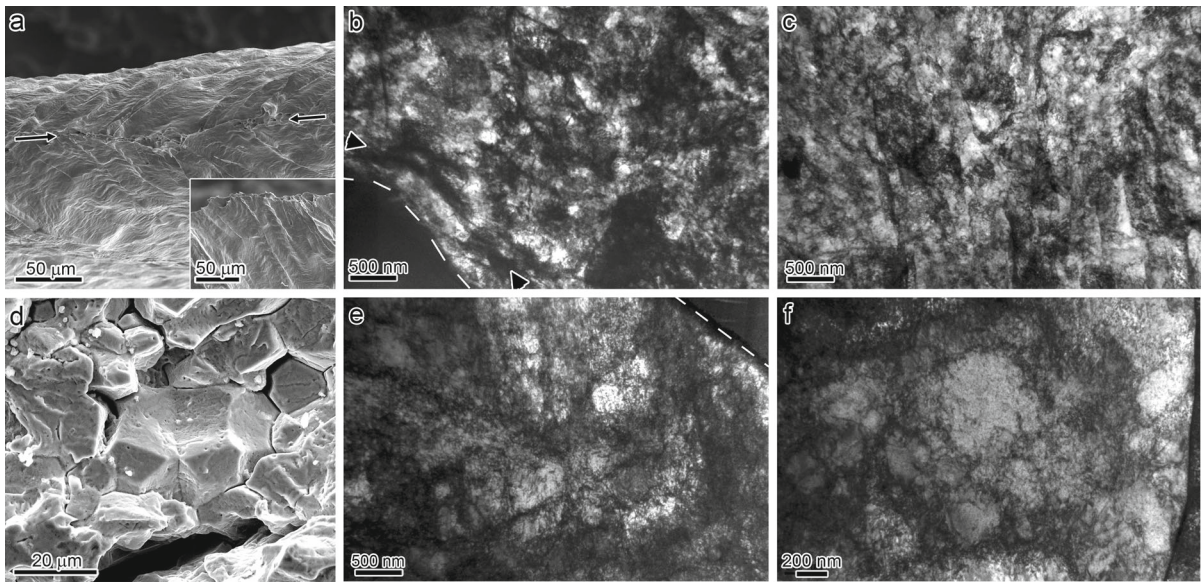


Fig. 4 Fracture of commercially pure iron for uncharged specimen (**a–c**) and hydrogen-charged specimen to 25.8 appm hydrogen concentration (**d–f**). **a, d** SEM micrographs of fractured surface, **b, e** TEM micrographs immediately below the fracture sur-

faces illustrated by the *dashed lines*, and **c, f** TEM micrographs about 5 μm below the fracture surfaces. The fracture strains for the uncharged and hydrogen-charged samples were 28 and 5 %, respectively (Wang et al. 2014)

3.2 Intergranular fracture of iron

Fracture surfaces of iron and low alloy steels failed in the presence of hydrogen are usually characterized as transgranular, consisting of microvoids and “quasi-cleavage” features. However, under high hydrogen concentration charging conditions, such as high current density cathodic charging, iron and steels may fail intergranularly (Jones 1990; Shin and Meshii 1983). Wang et al. (2014) studied the hydrogen-induced intergranular fracture of commercially pure iron. In their experiment, repeated stress-relaxation tests were conducted in the presence and absence of hydrogen on tensile specimens. The samples were first strained to 5 % above the initial yielding followed by 30 s relaxation, i.e. holding the specimen under constant displacement for 30 s. After this time, the specimens were pulled to restore the stress to the level before the relaxation step. The stress relaxation and restoring processes were repeated until the relaxation stopped. Some tensile specimens were cathodically charged during the test with a high current density where the hydrogen concentration was estimated to be about 25.7 appm. However, due to short period of the test no damage was observed on the

surfaces or grain boundaries of the hydrogen-charged samples.

The relaxation of stress stopped after 3 cycles for the hydrogen-free specimen. However, the hydrogen-charged specimen demonstrated relaxation until it was fractured after 19 relaxation cycles. It showed that while dislocations became immobile after 3 cycles in the absence of hydrogen, the dislocations in the hydrogen-charged samples were mobile until fracture. For the charged samples, the calculated mobile dislocation density after 3 cycles was about 84 % of the mobile density before the start of relaxation process; a clear indication for increased mobility of dislocations in the presence of hydrogen. Comparison of the microstructures of iron in the uncharged and hydrogen-charged specimens at a strain of 5 % showed that the dislocation densities were not significantly different, but in the presence of hydrogen, dislocations were more organized.

Figure 4 shows the result for fracture of iron in the presence and absence of hydrogen. Fracture mode changes from ductile void growth in the absence of hydrogen (Fig. 4a) to intergranular fracture in the presence of high hydrogen concentration (Fig. 4d). Using the FIB lift-out method, Wang et al. (2014)

extracted samples normal to the fracture surfaces of the uncharged and hydrogen-charged specimens. Investigating the microstructures below the fracture surface of the uncharged sample failed at 28 % strain showed high dislocation density formed into microbands but the microstructure was clearly changed from immediately below fracture surface (Fig. 4b) to about 5 μm below the fracture surface (Fig. 4c). For the hydrogen-charged specimen at fracture strain of 5 %, microstructure immediately and about 5 μm below the fracture surface are shown in Fig. 4e, f, respectively. The dislocations are organized into cell structures with dimensions in order of 500 nm immediately under the fracture surface while the cells were non-uniform 5 μm below the surface.

As discussed in Sect. 5.1, although decohesion is the failure process for intergranular fracture, hydrogen-induced decohesion alone without hydrogen-enhanced plasticity process is not sufficient to trigger a failure in iron. Therefore, Wang et al. (2014) proposed that the intergranular failure of iron in the presence of hydrogen is a plasticity-mediated process and the onset of failure is established by grain boundary structure and hydrogen content as well as local stress state which all have been affected by hydrogen-enhanced plasticity.

3.3 Hydrogen-induced intergranular and “quasi-cleavage” fractures of lath martensitic steel

Lath martensitic steel is the most common microstructure used in high strength steels for its excellent combinations of strength and toughness. The microstructure of a lath martensitic steel is complex: it consists of prior austenite grains divided into packets that are subdivided

into blocks of martensite laths. It should be noted that high strength steels are more susceptible to hydrogen embrittlement.

Nagao et al. (2012, 2014a, b) studied the effect of hydrogen on fracture of a middle carbon ultra-high strength martensitic steel that was a modified variation of AISI 4140 steel. The effect of adding additional elements to the steel is also investigated by considering a Ti-added steel while the baseline steel did not have any Ti. Single edge notch specimens of the lath martensitic steels were used in four-point bend testing. The specimens were first electroplated with a zinc layer to prevent outgassing of hydrogen after hydrogen charging and during the test. Then the specimens were thermally charged in high pressure hydrogen gas of either 31 or 138 MPa. The diffusible hydrogen (first peak hydrogen content in thermal desorption analysis) was measured for each charging pressure and steel.

The single edge notch bending tests on hydrogen-free and hydrogen-charged samples were conducted at a displacement rate of 0.1 $\mu\text{m/s}$ until fracture at room temperature. Hydrogen not only changed the fracture mode, it also changed the location of the fracture initiation sites (Nagao et al. 2014a). The fracture initiation sites for the hydrogen-free specimens were at the notch root, but the fracture of the hydrogen-charged samples initiated ahead of the notch root indicating that hydrogen changed the fracture of the lath martensitic steel from strain-controlled fracture to stress-controlled fracture. The fracture mode in the absence of hydrogen was ductile microvoid coalescence. However, the fracture surface of the hydrogen-charged steels was dominated by the “quasi-cleavage” features (Fig. 5a). Whereas the hydrogen-induced fracture surface of the baseline steels had some “flat” morphological features,

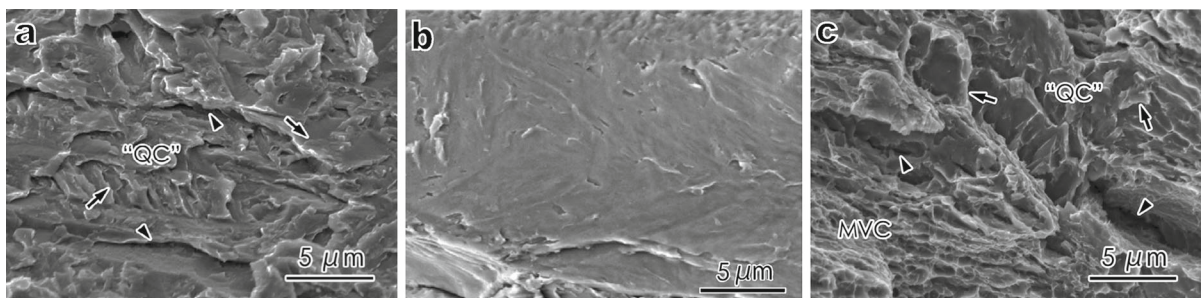


Fig. 5 SEM micrographs of hydrogen-induced fracture surfaces of tempered lath martensitic steel **a** “quasi-cleavage (QC)” features in the baseline steel, **b** “flat” features in the baseline steel,

and **c** “quasi-cleavage (QC)” and microvoid coalescence (MVC) features in the Ti-added steel (Nagao et al. 2012, 2014a)

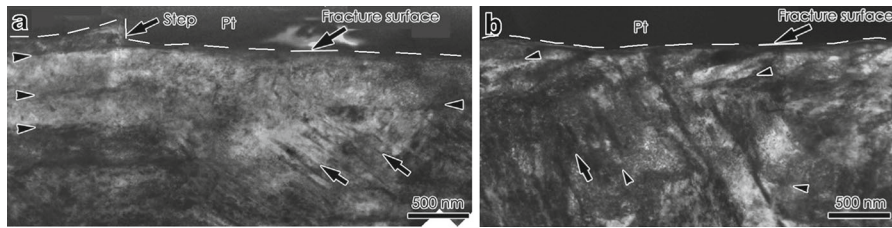


Fig. 6 TEM micrographs showing microstructure immediately under, **a** the “quasi-cleavage” morphology and **b** the flat morphology of the hydrogen-induced fracture surface of a tempered lath

martensitic steel. *Arrowheads* show the lath boundaries, *arrows* indicate slip bands and the *dashed lines* demonstrate the fracture surfaces (Nagao et al. 2012)

as shown in Fig. 5b, such features were absent in Ti-added steels. Instead, as shown in Fig. 5c, some microvoid coalescence morphologies were observed on the surface of hydrogen-charged Ti-added steels. Evidence of plastic deformation was observed for all hydrogen-induced fracture morphologies with small tear ridges, serrated markings and secondary cracks that show local plasticity.

In order to compare the effect of hydrogen on the mechanical properties, Nagao et al. (2012, 2014a) evaluated the nominal stress for hydrogen-free and hydrogen-charged specimens during the bending tests. The nominal stress is the bending stress experienced by a hypothetical straight beam with the height equal to the uncracked ligament size under the measured bending moment. The maximum nominal stress of the hydrogen-charged baseline steels was reduced by about a factor of 4 for the specimens charged in both 31 and 138 MPa hydrogen gas denoting that hydrogen degradation effects reached a saturation level under these hydrogen charging pressures. While in the absence of hydrogen the maximum nominal stress was the same for the Ti-added and the baseline steels, for the samples charged in 31 MPa hydrogen gas, the maximum nominal stress of the Ti-added specimens was higher than that of the baseline steel specimens. It showed that adding Ti can improve the hydrogen resistance of tempered lath martensitic steel. Nevertheless, the maximum nominal stress of the Ti-added steels charged in 138 MPa hydrogen gas dropped to the same value for the baseline steels.

In order to understand the origin of the features on different fracture surfaces and their relations with the microstructures immediately beneath the fracture surfaces, Nagao et al. (2012, 2014a, b) used the FIB lift-out technique to extract TEM samples below the observed fracture morphologies. Figure 6 shows the microstructures

below hydrogen-induced “quasi-cleavage” and flat surfaces in the baseline steel. The “quasi-cleavage” fracture surface (Fig. 6a) was along the lath boundaries whereas the flat surface fracture (Fig. 6b) was determined to be along the prior austenite grain boundary. Therefore, the flat features on the fracture surface of this martensitic steel actually denoted intergranular fracture. The common feature for the microstructure below these “quasi-cleavage” and flat surfaces was the intense slip bands (deformation band) (arrows in Fig. 6) such that the lath boundaries are partially destructed (arrowheads in Fig. 6). The slip bands for both flat and “quasi-cleavage” fracture were inclined to the fracture surface.

For the Ti-added steel, the microstructure beneath the “quasi-cleavage” fracture surface was similar to the one observed in the baseline steel. TEM samples extracted below microvoids in the uncharged and the hydrogen-charged Ti-added steels showed qualitatively similar heavily deformed microbanded structure with a high density of dislocations within the microbands (Nagao et al. 2014a).

Low temperature fracture was also investigated for the tempered lath martensitic steel. The fracture surface appeared to be similar to the hydrogen-caused “quasi-cleavage” surface but the fracture path was along the cleavage plane ($\{100\}$ -type). However, the microstructure below the fracture surface was very similar to the original undeformed microstructure with almost no change in the lath structure or dislocation density (Nagao et al. 2012).

Nagao et al. (2012, 2014a, b) proposed that hydrogen, by enhancing the dislocation mobility, increased the dislocation density close to the prior austenite grain and lath boundaries which consequently caused an increase in hydrogen concentration and reduced the cohesive energy of the boundaries, and created a con-

dition for nucleation and propagation of a crack on the boundaries. For the Ti-added steel, the primary difference between its microstructure and that of the baseline steel was determined to be the presence of the nanosized (Ti, Mo)C precipitates in the Ti-added steel. They explained that these precipitates increased the resistance of Ti-added steel to hydrogen embrittlement by trapping hydrogen and reducing hydrogen transported by mobile dislocations to degradation sites. At high enough hydrogen charging pressures, the (Ti, Mo)C precipitates were saturated with hydrogen and the trapping function did not work. The susceptibility of the Ti-added steel to hydrogen embrittlement was, therefore, the same as that in the baseline steel.

4 Hydrogen-induced fatigue fracture

4.1 Hydrogen enhanced fatigue crack growth of stainless steels

An important type of structural material considered to be more resistant to hydrogen embrittlement is fcc stainless steel. Being very expensive, stainless steels are usually used in small components exposed to hydrogen and not in a widespread pipeline networks. However, hydrogen can still accelerate fatigue crack growth in these steels.

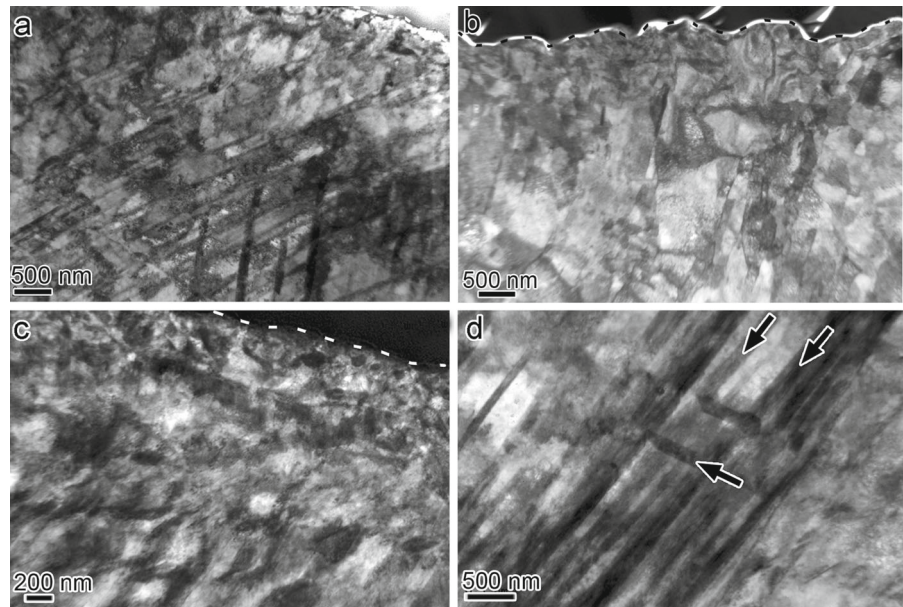
Martin et al. (2013) studied the effect of hydrogen on surface morphology and microstructure below 304 and 316 fcc stainless steels failed under fatigue loading conditions. The 316 stainless steel is an example of stable austenitic steel, while the 304 is unstable, with some of the austenite converting to martensite after deformation. The microstructure beneath fatigue fracture surface striations in 304 and 316 stainless steels both in the presence and in the absence of hydrogen was compared using TEM samples extracted by FIB lift-out technique from site-specific locations. The fatigue tests were performed using a tensile bar with a hole acting as a crack initiation site (Murakami et al. 2010). The applied fatigue load was 280 MPa fully reversed ($R = -1$) at a frequency of 1 Hz. The hydrogen-charged and uncharged samples were tested in air. A 304 stainless steel sample was also tested in 10 MPa pressure hydrogen gas. The hydrogen concentration in charged specimens was calculated to be 558 appm.

By examining the fracture surfaces through SEM, Martin et al. (2013) showed that hydrogen reduced the striation height and the distance between striations in both stainless steels. For the microstructures beneath the 304 and 316 stainless steel fracture surfaces, they observed a general refinement of the microstructure near the fracture surface irrespective of the test environment. The complexity of the microstructure decreased with distance from the fracture surface. However, the presence of hydrogen modified and refined the microstructure to an extent greater than achievable in its absence.

TEM analysis of microstructures below fracture surface of 304 stainless steel fatigued in the presence of hydrogen showed a layer 0.5–1 μm thick at the surface consisting of fine (~ 50 –200 nm) sub-grains with a few degree of misorientation between adjacent sub-grains. Below the sub-grains were microstructures with sets of intersecting deformation bands and dislocations (Fig. 7a). Diffraction analysis suggested that these bands are laths of strain-induced α' martensite localized closer to the crack tip with increasing hydrogen. The uncharged 304 stainless steel samples tested in air showed also a grain refinement below the fracture surface, as shown in Fig. 7b. However, unlike the thin layer in the hydrogen-charged samples, this refinement was extended for over 15 μm in depth with the larger sub-grain size (~ 500 nm) in uncharged samples. The sub-grains were predominantly martensite, though some austenite remained which showed that most of the material beneath the fracture surface was transformed to martensitic structure.

In the case of the 316 stainless steel in the presence of hydrogen, the microstructure below fatigue fracture surface was fundamentally similar to that in the 304, i.e. there was a 1 μm layer of fine sub-grains immediately beneath the fracture surface and beneath that layer was a microstructure consisting of dislocations and planar band features as shown in Fig. 7c, d. However, in a marked contrast with the 304 stainless steel, the bands in the 316 were not martensite; they appeared to be twins or overlapping stacking faults. Martin et al. (2013) mentioned that the microstructure of uncharged 316 sample showed refinement in the form of deformation bands parallel to the fracture surface similar to that deformed to high level of strains by rolling (Hughes and Hansen 2003). Further away from the fracture surface a complicated structure consisting of bands inclined to the fracture surface existed. Additionally, based on the

Fig. 7 TEM micrograph showing microstructure below striation of **a**, **b** 304 stainless steel and **c**, **d** 316 stainless steel. **a** Microstructure immediately below the fracture surface fatigued in 10 MPa hydrogen gas consisting of fine sub-grain and planar features. **b** Fine sub-grains immediately below the fracture surface of an uncharged sample tested in air. **c** Fine sub-grains immediately below the fracture surface of hydrogen-charged 316 stainless steel, and **d** planar features about 5 μm below fracture surface (Martin et al. 2013)



high level of observed refinements, they postulated that hydrogen not only modified the refined structure but stabilized microstructural configurations to an extent not achievable in its absence.

In order to understand the microstructural evolution under fatigue loading condition, Martin et al. (2013) extracted TEM samples ahead of arrested fatigue cracks. Within 1 μm of the crack tip, planar features were existed along with dislocation structures. About 5 μm ahead of the crack tip only dislocation structures were observed. They suggested that ahead of the crack tip, dislocation structures formed first. Then, as the crack approached, the dislocation structures changed to planar structures. With crack getting closer, the material was strained so much that immediately ahead of the crack tip the microstructure was disrupted by formation of a fine grain layer.

4.2 Fatigue crack growth in hydrogen gas with impurities

Fatigue crack growth rate of ferritic steel in hydrogen gas environment can be one or two orders of magnitude higher than that in air (Cialone and Holbrook 1988; San Marchi and Somerday 2012). However, it is shown that this hydrogen enhanced crack growth can be mitigated or even prevented by introducing some trace gases such

as carbon monoxide or oxygen in the hydrogen gas (Holbrook et al. 2012).

Somerday et al. (2013) studied the effect of mechanical and environmental variables on fatigue crack growth of X52 line pipe steel in hydrogen gas. Compact tension specimens were precracked in air before performing fatigue crack growth tests in 21 MPa hydrogen gas containing different levels of oxygen impurities ranging from negligible to 1000 vppm. The crack growth rate was then measured for different stress intensity factor ranges ΔK , with the load cycle frequency ranging from 0.001 to 10 Hz, and R-ratio (the ratio of minimum load to maximum load) of 0.1 or 0.5.

Fatigue crack growth in high-purity hydrogen gas (<0.5 vppm O_2) showed a threshold for activation of hydrogen-accelerated fatigue crack growth rate (Fig. 8). While for $\Delta K < 7.5 \text{ MPa}\sqrt{\text{m}}$ and $R = 0.1$ the crack growth rate per cycle da/dN was the same as that in air, the rate of crack growth abruptly increased with increasing ΔK . This was in agreement with Suresh and Ritchie (1982) in which the onset of acceleration is associated with a critical maximum stress intensity factor K_{max} . In the presence of oxygen impurities in hydrogen gas, da/dN versus ΔK with $R = 0.1$ for the X52 steel exhibited similar behavior but the onset of acceleration was shifted to higher values of ΔK with increasing oxygen concentration to 100 or 1000 vppm

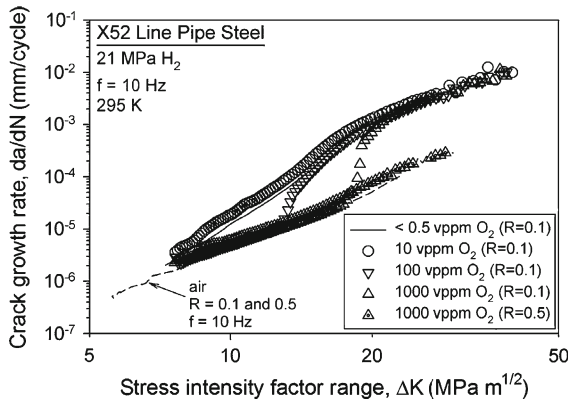


Fig. 8 Experimental results of fatigue crack growth rate da/dN versus stress intensity factor range ΔK with $R = 0.1$ and 0.5 for X52 line pipe steel in 21 MPa high-purity hydrogen gas (<0.5 vppm), in 21 MPa hydrogen gas with various concentration of oxygen impurity, and in air (Somerday et al. 2013)

as shown in Fig. 8. The onset for enhanced fatigue crack growth rate in hydrogen gas with 10 vppm oxygen was the same as that in high-purity hydrogen environment showing no effect of oxygen at this small concentration in hydrogen gas. Figure 8 also shows that the fatigue crack growth test with $R = 0.5$ in hydrogen gas with 1000 vppm oxygen impurity did not exhibit the acceleration of crack growth in the ΔK range tested.

The effect of load cycle frequency on fatigue crack growth was also investigated by Somerday et al. (2013). Fatigue crack growth rate in air was independent of the frequency. In high-purity hydrogen gas environment, however, at lower load cycle frequencies the crack growth rate was accelerated relative to air but independent of frequency. In contrast, in hydrogen gas with oxygen impurities, as frequency decreased the hydrogen-accelerated crack growth rate diminished, eventually converging with crack growth rates in air.

Somerday et al. (2013) also developed a model to describe the onset of hydrogen-accelerated fatigue crack growth. Since the chemisorption of oxygen on iron surfaces does not have an activation barrier (Staykov et al. 2014), it is assumed that upon exposure to enough oxygen molecules, the crack surface is passivated to impede the ingress of atomic hydrogen. Then hydrogen can only enter through the newly created surfaces at the crack tip as the fatigue crack extends. Therefore, the competition between creation of the new surfaces and their passivation by oxygen determined the onset of hydrogen-accelerated fatigue crack growth. It is assumed that diffusion of oxygen

molecules through hydrogen gas in the crack channel to the newly created crack-tip surface during one load cycle controlled the oxygen adsorption and passivation of the surface. If the oxygen coverage of the crack-tip surface during the load cycle was less than a critical level, hydrogen uptake at the crack tip enhanced the fatigue crack growth. An analytical expression was presented for the onset of hydrogen-accelerated crack growth as a function of load cycle frequency, R -ratio, oxygen concentration in hydrogen gas and rate of fatigue crack growth in air. This was the first time that a single formula was proposed for describing the oxygen effect on hydrogen-accelerated fatigue crack growth in terms of all parameters that govern this complex phenomenon.

5 On the fundamentals of hydrogen-induced fracture

5.1 Hydrogen effect on the reversible work for grain boundary separation in a gaseous environment

According to the classical Gibbs adsorption isotherm, hydrogen-induced changes to the free surface (FS) energy γ_{FS} and the grain boundary (GB) energy γ_{GB} vary linearly with changes to the chemical potential of hydrogen (Hirth and Rice 1980; Rice and Wang 1989; Kirchheim 2007):

$$\begin{aligned} d(\gamma_{FS}) &= -\Gamma_H^{FS} d(\mu_H^{FS}) \\ d(\gamma_{GB}) &= -\Gamma_H^{GB} d(\mu_H^{GB}) \end{aligned} \quad (1)$$

where $\Gamma_H^{FS/GB}$ is the excess of hydrogen on the FS or GB area and $\mu_H^{FS/GB}$ is the chemical potential of hydrogen on the FS or GB. The change of the grain boundary cohesive energy (or reversible work of separation) $d(2\gamma_{int})$ can be calculated through

$$d(2\gamma_{int}) = d(2\gamma_{FS}) - d(\gamma_{GB}). \quad (2)$$

In the case that it is energetically favorable for the H atoms to reside on the FS rather than on the GB, i.e. $d(2\gamma_{FS}) < d(\gamma_{GB})$, hydrogen embrittles the grain boundary. An alternative way to characterize the potency of hydrogen for GB embrittlement is (Wu et al. 1994; Zhong et al. 2000):

$$\Delta E_{em} = E_{GB}^{seg} - E_{FS}^{seg} > 0, \quad (3)$$

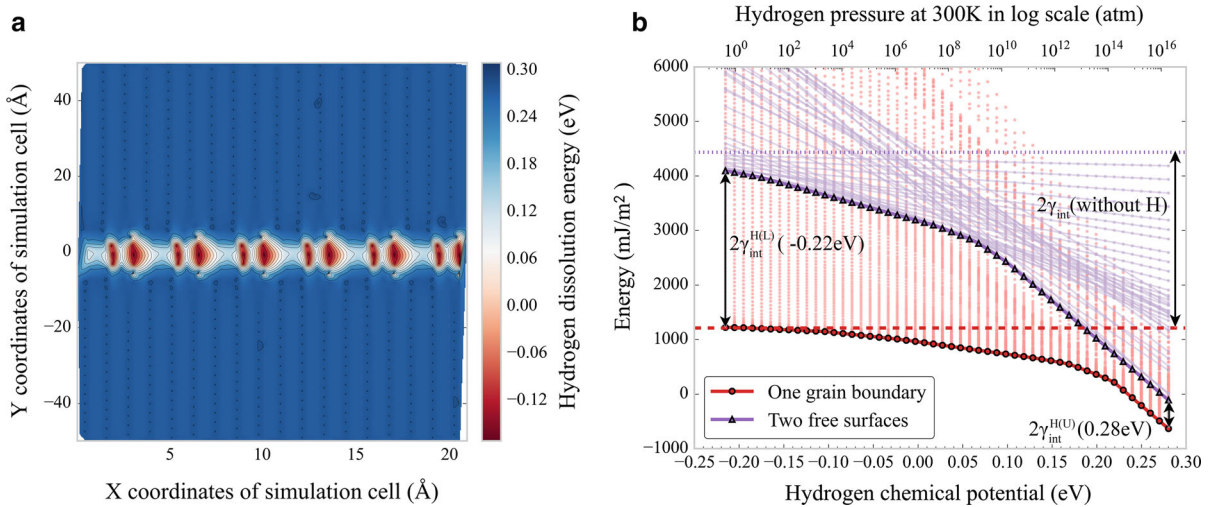


Fig. 9 The hydrogen effect on the energies of a $\Sigma 3(111)$ GB, the associated (111) FS, and the reversible work of separation of the GB. **a** The H dissolution energy map for a $\Sigma 3(111)$ GB with the energy levels on the color bar denoted in eV. **b** The grain boundary energy γ_{GB} and free surface energy $2\gamma_{FS}$ upon separation plotted as functions of the H chemical potential for a $\Sigma 3(111)$ GB. The maximum number of H solute atoms is 74

where E_{GB}^{seg} and E_{FS}^{seg} are the segregation energies of hydrogen on the GB and FS, respectively. For the bcc Fe-H system, the embrittlement potency for $\Sigma 3(111)\langle 110 \rangle$ GB was calculated to be +0.26 eV (25.21 kJ/mol) (Zhong et al. 2000) which implies that hydrogen weakens the GB and hence, if fracture takes place reversibly can be intergranular. However, even under high hydrogen gas pressures, the predominant failure mode of Fe in the presence of hydrogen is transgranular. As mentioned before, the intergranular fracture of iron was only reported under specific cathodic charging conditions upon which markedly higher amounts of hydrogen can be injected into the material than upon charging in a hydrogen gas environment (Jones 1990; Shin and Meshii 1983; Wang et al. 2014).

Wang et al. (2015) investigated over 105 types of bcc Fe GB (50 types of $\langle 100 \rangle$ and 55 types of $\langle 110 \rangle$ symmetric tilt boundaries with different orientation angles) as well as the corresponding 105 FS structures using molecular static calculations with a density functional theory based empirical potential. They obtained the energetically favorable locations of the hydrogen atoms on the FS and GB over a range of hydrogen environmental pressures. For each grain boundary, Wang

corresponding to 87.31/nm² FS or GB excess. The horizontal dashed and dotted lines denote respectively the GB energy γ_{GB} and the free surface energy $2\gamma_{FS}$ in the absence of hydrogen. The separation distance between the grain boundary and the free surface lines indicates the reversible separation work ($2\gamma_{int}$). The corresponding pressure at 300 K is shown in upper x-axis (Wang et al. 2015)

et al. determined the equilibrium H excess on the GB and FS associated with the lowest GB and FS energies at a given H chemical potential. More specifically, Wang et al. first found the dissolution energy for all possible positions of hydrogen on each GB and FS. A typical dissolution energy map for $\Sigma 3(111)$ GB is shown in Fig. 9a. From this energy map, it is possible to configure initial atomic configurations of GB and FS with different number of H atoms (initial H excesses), according to a scheme whereby the lowest dissolution energy sites (strongest traps) are filled first and those with higher energies are filled next. The calculations were carried out over a range of chemical potentials of H bounded from below by $\mu_H^{H(L)}(T, P)$, at which H just started to be trapped on the GB, and from above by $\mu_H^{H(U)}(T, P)$, at which the GB is saturated and lattice T-sites begin to get filled out. The latter case of saturated GB is consistent with the classical model (Rice and Wang 1989; Wu et al. 1994; Zhong et al. 2000), however, it may not be experimentally attainable due to the required very high value of chemical potential (Wang et al. 2015). For the molecular statics calculations, $\mu_H^{H(L)}(T, P)$ equals −0.22 eV and $\mu_H^{H(U)}(T, P)$ equals 0.28 eV.

For an assumed initial H excess, grain boundary energies $\gamma_{GB}^{H(L)}$ and $\gamma_{GB}^{H(U)}$ were calculated at chemical potentials $\mu_H^{H(L)}(T, P)$ and $\mu_H^{H(U)}(T, P)$, respectively. In a graph of γ_{GB} versus μ_H , a straight line connecting these two points represents the relationship between the GB energy and the chemical potential for a given H excess in accordance with Eq. (1). By repeating this process for several hydrogen excess values, a series of γ_{GB} versus μ_H lines were obtained for representing all possible Fe-H atomic configurations between $\mu_H^{H(L)}(T, P)$ and $\mu_H^{H(U)}(T, P)$. For a given chemical potential, the minimum energy configuration is the energetically favorable GB-H atomic configuration, thus the equilibrium H excess is obtained. The same approach was used to obtain the energetically favorable configurations for the FS-H system. Then, the reversible work of separation of the grain boundary for a given H chemical potential can be obtained through $2\gamma_{int}^H = (2\gamma_{FS}^H)_{min} - (\gamma_{GB}^H)_{min}$. The chemical potential was linked to the hydrogen pressure in the environment through $\mu_H(T, P) = \mu_H(T, P_0) + 1/2kT \ln(P/P_0)$, in which k denotes the Boltzmann constant, $P_0 = 1$ atm, and the values of $\mu_H(T, P_0)$ can be found in the JANAF thermochemical tables (Stull and Prophet 1971).

A typical plot of γ_{GB} versus μ_H for a $\langle 110 \rangle$ symmetric tilt $\Sigma 3(111)$ GB is shown in Fig. 9b. The upper x-axis denotes the hydrogen gas pressure at 300 K. The lead and the tail of the semi-transparent dotted lines (GB) and solid lines (FS) are the $(\mu_H^{H(L)}, \gamma_{GB/FS}^{H(L)})$ and $(\mu_H^{H(U)}, \gamma_{GB/FS}^{H(U)})$ points, respectively. The points between them denote interpolated values from Eq. (2), indicating the energies at different chemical potentials (or hydrogen gas pressures on the upper axis). The minimum energy configurations (lowest FS and GB energies) are represented by the “one GB” line in Fig. 9b and the “two FS” line, respectively. The “two FS” line represents the magnitude of the FS taken twice and thus the GB cohesive energy is denoted by the separation distance between the “one GB” line and “two FS” line. From the “two FS” line, one can deduce that the FS has an almost constant excess of H at hydrogen chemical potential lower than 0.05 eV. At higher chemical potentials, the equilibrium FS H excess becomes $87.31/\text{nm}^2$ which represents saturation. At pressure lower than 10,000 atm, the GB accommodates much lower hydrogen excess values than the FS, and the assumption that the GB and FS have the same coverage (Rice and Wang

1989; Wu et al. 1994; Zhong et al. 2000) is only valid at extremely high pressures (10^{16} atm).

The calculations of Wang et al. (2015) indicate that the cohesive energy in hydrogen gas at 1000 atm and 300 K (H chemical potential = -0.12 eV) is not reduced by more than 33 % of the cohesive energy in the absence of hydrogen for all 105 GB types studied, whereas at $\mu_H^{H(U)}(T, P) = 0.28$ eV, a maximum reduction by 92 % was found for a $\Sigma 13(230) \langle 100 \rangle$ grain boundary. The use of the reversible work of separation at chemical potential $\mu_H^{H(U)}(T, P)$ to ascertain the grain boundary strength is consistent with the classical model of Rice and Wang (1989), but according to the present calculations, this model only applies for pressures between 10^{14} atm and 10^{16} atm, i.e. along the linear part of the curves at the bottom right hand side of Fig. 9b. Considering the moderate reductions of the reversible work of separation of a grain boundary by hydrogen at pressures prevalent in real-world hydrogen embrittlement situations, we conclude that whereas the reduction of the cohesive energy by hydrogen is a contributing factor to hydrogen-induced intergranular failure of Fe it may not be the sole cause of embrittlement. Moreover, during the dynamic failure process, the GB hydrogen excess cannot be sustained at a constant level; grain boundary defects and local plasticity around the grain boundary play important roles in interacting with the decohesion process.

5.2 Modeling hydrogen transport by dislocations

The study of the microstructures beneath the hydrogen-induced fracture surfaces (Martin et al. 2011a, b, 2012, 2013; Nagao et al. 2012, 2014a; Wang et al. 2014) presented earlier demonstrated the enhanced evolution of dislocation structure which was extended far from the fracture surfaces into deforming material. Those observations along with the required hydrogen accumulation for decohesion suggested that the dislocation transport of hydrogen should enhance local hydrogen concentration at initiation sites (e.g. grain boundaries) which led to final fracture.

Dadfarnia et al. (2015) developed a dislocation mediated transport model which takes into account the hydrogen transport by mobile dislocations as well as hydrogen trapping and stress-driven hydrogen diffusion. In order to incorporate the hydrogen-enhanced dislocation generation and hydrogen-enhanced dislo-

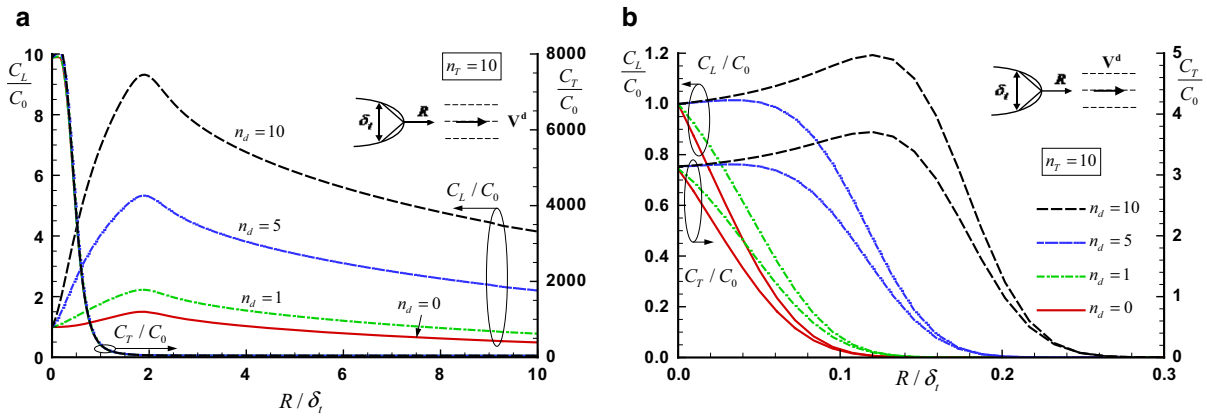


Fig. 10 Normalized lattice hydrogen concentration C_L/C_0 and normalized trapped hydrogen concentration C_T/C_0 ahead of the crack tip versus normalized distance R/δ_t at $K_I = 100 \text{ MPa}\sqrt{\text{m}}$ with the direction of the dislocation velocity vector V^d with respect to the crack plane shown in the figure for **a** the bcc steel and **b** the fcc steel. The parameter δ_t is the crack opening displacement and C_0 is the lattice hydrogen concentration at the crack tip

cation velocity in elastoplastically deforming materials, a simple approach was adopted by using multiplying factors of n_T and n_d for dislocation traps and dislocation velocity, respectively. Parametric studies were conducted for n_T and n_d to study the effect of hydrogen-induced dislocation density and velocity.

The developed model was used in finite element framework to simulate transient hydrogen transport ahead of a crack tip representing hydrogen uptake and transport around a crack in a material under rising load in hydrogen gaseous environment. The numerical solutions were obtained for a model X70/X80 line pipe bcc steel and a model forged 21Cr-6Ni-9Mn austenitic fcc stainless steel representing low solubility/high diffusivity system and high solubility/low diffusivity system, respectively. The specimen was loaded to $100 \text{ MPa}\sqrt{\text{m}}$ under plane strain small scale yielding conditions with hydrogen concurrently diffusing from the crack surface into the initially hydrogen-free bulk material around the crack tip. Figure 10 shows the effect of dislocation transport on the development of hydrogen concentration at normal interstitial lattice, C_L , and trapping sites, C_T , ahead of the crack tip. In the results presented in this figure, it is assumed that the dislocation slip planes are parallel to the crack plane as shown in the figure sub-sets. The lattice and trapped hydrogen concentrations are normalized by the lattice hydrogen concentration at the crack tip, C_0 , assumed to be in equilibrium with

hydrogen gas at 1 atm. The parameters n_T and n_d denote the effect of hydrogen respectively on dislocation density and velocity during plastic straining. For the bcc steel, $\delta_t = 48.16 \mu\text{m}$ and $C_0 = 2.084 \times 10^{21} \text{ H atoms/m}^3$ (0.0246 appm) and for the fcc steel $\delta_t = 40.99 \mu\text{m}$ and $C_0 = 7.996 \times 10^{24} \text{ H atoms/m}^3$ (94.4 appm) (Dadfarnia et al. 2015)

hydrogen gas at 1 atm, and the distance ahead of the crack tip R is normalized by the crack tip opening displacement δ_t at $K_I = 100 \text{ MPa}\sqrt{\text{m}}$. The results for $n_d = 0$ represent no hydrogen transport by dislocations. As shown in Fig. 10, dislocation transport had a marked effect on accumulation of hydrogen concentration ahead of the crack tip. The model showed that dislocation transport can deliver hydrogen at distances further afield and at larger concentrations than lattice diffusion alone.

5.3 Thermal desorption analysis (TDA)

Hydrogen resides in materials either at normal interstitial lattice sites (NILS) or at trapping sites. Defects such as dislocations, grain boundaries, precipitates, inclusions, vacancies can be hydrogen trapping sites. Measuring hydrogen content and also determining hydrogen trapping sites and the binding energy of hydrogen to the corresponding traps are indispensable for a correct understanding of hydrogen distribution in materials, which is closely related to the fracture mechanics of hydrogen embrittlement.

TDA is often used to obtain these data (Li et al. 2004; Novak et al. 2010). In the literature the term thermal desorption spectroscopy (TDS) is also used interchangeably with TDA. A specimen is heated at

a constant rate and the hydrogen concentration is measured with a gas chromatograph or a mass spectrometer as a function of temperature; then the measured hydrogen concentration is normalized as hydrogen desorption rate. A thermal conductivity detector (TCD) or a quadrupole mass spectrometer is most commonly used as the hydrogen detector for the gas chromatography and the mass spectrometry, respectively. Obtaining accurate and reproducible TDA data requires an appropriate calibration of hydrogen concentration and strict control on sample handling protocols that consist of sample preparation (specimen size, specimen surface condition), hydrogen charging condition (solution/gas, temperature, duration), time interval between the finish of hydrogen charging and the start of TDA and so on. Round-robin tests have been conducted in Japan to examine the effect of various experimental factors on TDA results (Suzuki and Takai 2012).

TDA data is normally taken from room temperature to some elevated temperature in accordance with the experimental purpose. However, hydrogen can escape from a specimen before the start of TDA at room temperature. This can be the case for hydrogen residing at NELS and low-binding energy trap sites. To explore the existence of such hydrogen, Takai and coworkers developed a new TDA system that can take data of hydrogen evolution from -200°C (Takai 2011; Abe et al. 2010, 2011). A quadrupole mass spectrometer is installed on their system. Examples of TDA spectra that were achieved using their system are presented in Fig. 11. They studied the effect of carbon content on hydrogen trapping behavior using pure iron and

a ferritic steel. The size of specimens they used was $10 \times 10 \times 0.3 \text{ mm}$; they took TDA spectra between -200 and 200°C at a heating rate of $1^{\circ}\text{C}/\text{min}$. Six peak temperatures are observed in the spectra: A = -120 , B = -105 , C = -50 , D = 0 , E = 20 and F = 75°C . Along with a microstructural study, they attributed the peak-A to NELS hydrogen. The peak-B corresponds to fragment hydrogen ions of water. Further, they attributed the peaks-C, -D and -E to hydrogen trapped at dislocations and asserted that increasing carbon content results in lower peak temperature. Furthermore, they assumed that the peak-F is from hydrogen trapped at carbides.

Hydrogen content is easily determined from a TDA spectrum given that an appropriate calibration of hydrogen concentration has been conducted. Terminologies of “peak-1 hydrogen content” and “peak-2 hydrogen content” are often used (Suzuki and Takai 2012). Peak-1 hydrogen normally means reversible hydrogen and peak-2 hydrogen is from irreversible hydrogen trap states. Reversible hydrogen normally infers hydrogen that is diffusible at room temperature. Total hydrogen is the sum of hydrogen contents from peaks-1 and -2. To measure the hydrogen content, a specimen of larger dimension is more suitable to minimize hydrogen egress before the start of TDA.

Determining hydrogen trapping sites and the binding energy of hydrogen to the corresponding traps requires a careful experiment and a following analysis. Numerical methodology to simulate a TDA spectrum is often helpful to derive accurate estimates. A standard method is that identically prepared specimens are heated at three or more different constant rates, then temperatures corresponding to the desorption rate peaks are numerically analyzed to calculate the activation energy of desorption for each trap site. The trap binding energy can be estimated by subtracting the activation energy for hydrogen diffusion from the calculated activation energy of desorption. The hydrogen trapping site can be identified from microstructural information. The comparison of the determined trap binding energy with previous data in literature is also beneficial to reach a correct conclusion about the identification of trap sites.

Upon heating, the binding between hydrogen and a trap site is loosened and hydrogen diffuses through the specimen and finally escapes through the surface. Two cases can be considered for the rate determin-

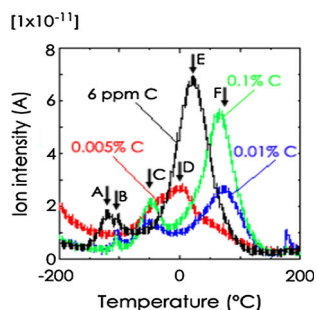


Fig. 11 Examples of thermal desorption analysis spectra from hydrogen-charged pure irons and a ferritic steel containing 6 mass ppm, 0.005, 0.01 and 0.1 mass % of carbon. Note that the spectra start with -200°C using a new TDA system developed by Takai and coworkers (Abe et al. 2010)

ing step for the thermal desorption process: thermal-detrapping and diffusion. In a case where hydrogen diffusion is faster than the release of hydrogen from a hydrogen trapping site, the hydrogen desorption profile can be modeled using the process of hydrogen release from the trap site; this case is regarded as the thermal-detrapping-determining desorption. The diffusion-determining desorption is an opposite case to the thermal-detrapping-determining desorption; hydrogen diffusion is slower than the detrapping process and thus, hydrogen diffusion is the rate determining step for the thermal desorption process.

The formula for the thermal-detrapping-determining desorption of hydrogen was originally proposed by Kissinger (1957). Choo and Lee (1982) proposed a derivative form of Kissinger's formula while taking into account a hydrogen atom being bound to a trap site. Further, Wei and Tsuzaki (2006) and Wei et al. (2012) proposed a modified model while taking into consideration hydrogen diffusion. Kirchheim (2014) also considered the effect of hydrogen diffusion through a specimen in his attempt to simulate TDA spectra.

In the case of the diffusion-determining desorption, local hydrogen equilibrium is held between NILS and trapping sites. The effective hydrogen diffusion constant under an assumption of a local equilibrium between lattice and trapped hydrogen was originally given by McNabb and Foster (1963). A general formulation developed by McNabb and Foster was later simplified by Oriani (1970). Ono and Meshii (1992) and Yamaguchi and Nagumo (2003) applied this simplified model to simulate TDA spectra. Their approach is only applicable to simulate TDA spectra with a single peak. Ebihara et al. (2007) expanded this model to simulate TDA spectra with multiple peaks by numerically imposing hydrogen local equilibrium postulate in the temperature raising process.

Furthermore, Ebihara et al. (2009) proposed a "fundamental" model to reproduce thermal desorption spectra of hydrogen regardless of the rate-determining process by describing mass conservation of hydrogen in a specimen with the activation energy law for diffusion, trapping and detrapping processes.

These numerical simulations are quite useful to determine peak temperatures. There are some cases where multiple peaks show up from an apparent single peak. The change of microstructure during the heating process such as disappearance of retained austenite or

vacancies can influence TDA spectra. An analysis for such a case has not been established yet.

6 Modeling intergranular crack initiation in hydrogen-charged high-strength steel

Reduction of the strength of a high-strength steel charged in hydrogen can occur with the change in fracture mode from ductile microvoid coalescence to intergranular fracture. Novak et al. (2010) developed a micromechanical model to explain hydrogen-induced intergranular cracking of AISI 4340 high-strength martensitic steel. The underlying assumption for their model was that fracture initiation was a result of decohesion at the grain boundary carbide/matrix interfaces.

Novak et al. (2010) assumed that decohesion of the interface of a grain boundary carbide was due to interfacial stress increased by the impingement of a dislocation pile-up onto a carbide particle and the reduction of the interface strength in the presence of hydrogen. They further assumed that the carbide/matrix interface decohesion produces microcracks propagating along the grain boundary as non-interacting flaws; thus they considered the weakest link statistics assumption valid and calculated the total survival probability of a material volume V as

$$1 - \Phi = \exp \left[-N \int_0^V \int_0^\sigma g(S) dS dV \right], \quad (4)$$

where σ is the local maximum stress, $\int_0^\sigma g(S) dS$ is the fraction of particles per unit volume with interfacial strength less than σ , and N is the number density of carbide particles that participate in the decohesion process.

The number of particles with interfacial strength less than σ was determined using the Smith model (Smith 1966) as

$$\frac{l}{d} S^2 + \tau_{eff}^2 \left[1 + \frac{4}{\pi} \frac{\tau_0}{\tau_{eff}} \sqrt{\frac{l}{d}} \right]^2 = \frac{\pi E \gamma_{eff}}{(1 - \nu^2) d}, \quad (5)$$

where l is the carbide size, S is the interface strength, d is the grain boundary size, τ_0 is the friction stress, $\tau_{eff} = \tau_e - \tau_0$ is the effective stress which is the difference between the applied shear stress $\tau_e = \sigma_e / \sqrt{3}$ (σ_e is the effective stress) and the friction stress τ_0 , E is the

elastic modulus, ν is the Poisson's ratio, and γ_{eff} is the work of fracture associated with the decohesion process of the carbide/matrix interface. The work of fracture is obtained from $2\gamma_{eff} = 2\gamma_{int} + \gamma_p$, where $2\gamma_{int}$ is the reversible work of separation and γ_p is the plastic work accompanying the separation (Jokl et al. 1980). The reversible work of separation is assumed to reduce in the presence of hydrogen according to the thermodynamic theory of decohesion of Hirth and Rice (1980) and the plastic work is considered to be a very steep function of the reversible work of separation according to Jokl et al. (1980). Thus, hydrogen greatly reduces the total decohesion energy of the carbide/matrix interfaces.

Novak et al. (2010) thermally charged single edge notch bend specimens of AISI 4340 steel in hydrogen gas under different pressures to obtain specimens with different amounts of charged hydrogen concentrations. The specimens were loaded with 0.1 $\mu\text{m/s}$ displacement rate until fracture. The fracture strength was evaluated in terms of the nominal stress which was calculated as the maximum bending stress experienced by a beam with height equal to the uncracked ligament size. They used thermal desorption spectroscopy and identified the three types of traps in AISI 4340 steel: dislocations, grain boundaries, and carbides with binding energies of 18, 48, and 72 kJ/mol, respectively (Hirth 1980).

In order to obtain the probability of failure, Novak et al. (2010) performed finite element analysis and solved the coupled hydrogen diffusion initial/boundary-value problem and the elastoplastic boundary problem during the displacement loading of the single notch bending specimens. Through finite element calculations, they determined the principal normal stress σ and hydrogen concentration which allowed for the calculation of the hydrogen effect on the effective fracture work γ_{eff} , the fraction of particles per unit volume with interfacial strength less than σ , i.e. $\int_0^\sigma g(S)dS$, and subsequently the probability of failure Φ for the specimen through Eq. (4). The failure load was identified as the load at which the total survival probability is $1 - \Phi = 50\%$. Figure 12 shows the prediction of the fracture model for the failure of the 4340 steel as a function of initial lattice hydrogen concentration (Novak et al. 2010). The superposed experimental data shows that the model successfully predicts the effect of hydrogen on the intergranular fracture of the 4340 steel.

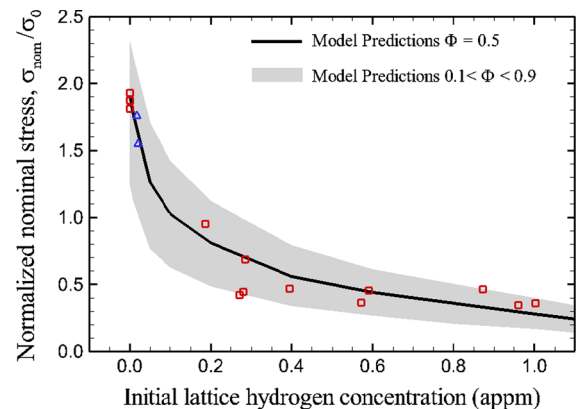


Fig. 12 The nominal fracture stress normalized by the initial yield stress, $\sigma_0 = 1490$ MPa, predicted by the model as a function of lattice hydrogen concentration. Data points show the experimental measurements (Novak et al. 2010)

7 Conclusions

We reviewed recent experimental and modeling efforts related to the study of hydrogen embrittlement of structural materials. The results demonstrated that plasticity processes are a fundamental part of hydrogen-assisted fatigue and fracture.

The experimental studies of the hydrogen-induced fatigue and fracture surfaces and the microstructure developed beneath them for different material systems were reviewed. Independent of fracture mode, crystal structure and charging method, the evolution of microstructures and dislocation structure were more advanced in the presence of hydrogen. The dislocation activity was widespread throughout the material and not confined to the fracture surface which was explained by the hydrogen-enhanced nucleation and mobility of dislocations and hydrogen shielding model. Another important point that one can draw from these experimental studies is that looking at the hydrogen-induced fracture surface is not sufficient in determining the deformation process prior to fracture or deciding about the origin of the features on the fracture surfaces.

The atomistic calculation of cohesive energy of the different grain boundaries in the presence of hydrogen showed that under typical experimental conditions for hydrogen gas environment the maximum reduction in the cohesive energy is about 30%. It was posited that the reduction of the cohesive strength of the boundary due to diffusive hydrogen only is not sufficient to

bring about failure and the impact of plasticity and enhanced dislocation activity should be considered. The modeling results along with experimental observations of the microstructure associated with hydrogen-induced intergranular fracture supported the conclusion that the hydrogen-enhanced local plasticity and attendant effects are able to establish the local conditions responsible for the transition in fracture mode from transgranular to intergranular. Hydrogen induced intergranular failure occurs by a reduction of the cohesive energy but with contributions from structural as well as compositional changes in the grain boundary. A model was also presented for hydrogen transport by mobile dislocations. The results of simulation showed that accounting for hydrogen enhanced dislocation mobility and nucleation can explain the delivery of hydrogen at larger concentrations at distances further afield by mobile dislocations than diffusional process alone.

These studies gave rise to a new proposed mechanism for hydrogen embrittlement: hydrogen-enhanced plasticity mediated failure mechanism. Hydrogen enhances the dislocation generation and mobility and at the same time dislocations carry and deposit hydrogen to potential fracture initiation sites. The failure is then initiated by the combination of stress elevation due to high dislocation density and weakening due to high hydrogen concentration. Therefore, according to this mechanism hydrogen-enhanced plasticity processes determines the condition for failure.

An approach was presented to mitigate the hydrogen effect on a ferritic system under cyclic loading. It was found that a few hundred molecules of oxygen per million molecules of hydrogen can eliminate the degradation effect of hydrogen. The result was explained through an analytical model based on the assumption that oxygen adsorption on the newly created surfaces prevents the hydrogen ingress to the material.

Lastly, a statistically-based micromechanical model for hydrogen-induced brittle intergranular fracture initiation was reviewed. The model accounts for the combined action of HELP and decohesion. The prediction of the model was compared with the experimental results from the embrittlement of 4340 high-strength martensitic steel. The results showed that this approach holds great promise for the prognosis procedures of the failure of structural materials in hydrogen.

8 Future research directions

In this paper we attempted to describe the current understanding of hydrogen-plasticity interactions with fracture processes and events. Although we reported significant advances, especially with regard to plasticity-mediated decohesion, development of models with predictive capabilities requires major breakthroughs in the following directions (Dadfarnia et al. 2010):

1. Measurement and calculation of the effect of hydrogen on grain boundary and interfacial cohesion.
2. Identification and measurement of the concentration of hydrogen at key microstructural features in structural materials such as dislocation cores, grain boundaries, and precipitates.
3. Quantification of the synergy between the hydrogen-enhanced localized plasticity and decohesion-based models of hydrogen embrittlement.
4. Critical evaluation of other proposed mechanisms of hydrogen embrittlement and determination of the conditions, if any, under which they are viable. This includes but is not limited to mechanisms such as the hydrogen-vacancy mechanism, the hydrogen-assisted dislocation emission, etc.

Acknowledgments This work was supported by the DOE EERE Fuel Cells program through Grant GO 15045. M.D., A.N., S.W., B.P.S., and P.S. acknowledge the support from the World Premier International Research Center Initiative (WPI), MEXT, Japan, through the International Institute for Carbon-Neutral Energy Research (I2CNER) of Kyushu University. S.W. acknowledges support from the National Science Foundation through Award No. CMMI-1406462. The authors would also like to acknowledge Prof. I.M. Robertson at the University of Wisconsin-Madison for his guidance, support and discussions. Also, the authors acknowledge K.E. Nygren at the University of Wisconsin-Madison for fruitful discussions.

References

- Abe N, Suzuki H, Takai K, Hagihara Y, Sueyoshi H, Ishikawa N (2010) Hydrogen desorption spectra of α -Fe including carbon using thermal desorption spectrometer detected from low-temperature. In: CAMP-ISIJ. The 159th Iron and Steel Institute of Japan (ISIJ) Meeting, Ibaraki, Japan, Mar 28–30, 2010, vol 23
- Abe N, Suzuki H, Takai K, Ishikawa N, Sueyoshi H (2011) Identification of hydrogen trapping sites, binding energies, and occupation ratios at vacancies, dislocations and grain boundaries in iron of varying carbon content. Materials Science and Technology (MS&T) 2011. The Minerals, Metals and Materials Society, Warrendale, PA, pp 1277–1284

- Beachem CD (1972) New model for hydrogen-assisted cracking (hydrogen embrittlement). *Metall Trans* 3(2):437–451. doi:[10.1007/BF02642048](https://doi.org/10.1007/BF02642048)
- Bechtel S, Kumar M, Somerday BP, Launey ME, Ritchie RO (2009) Grain-boundary engineering markedly reduces susceptibility to intergranular hydrogen embrittlement in metallic materials. *Acta Mater* 57(14):4148–4157. doi:[10.1016/j.actamat.2009.05.012](https://doi.org/10.1016/j.actamat.2009.05.012)
- Bernstein IM, Thompson AW (1984) The role of microstructure in hydrogen embrittlement. In: Gibala R, Hehemann RF (eds) *Hydrogen embrittlement and stress corrosion cracking*. American Society for Metals, Metal Park, OH, pp 135–152
- Birnbaum HK (1977) Hydrogen related failure mechanisms in metals. In: Foroulis ZA (ed) *Environmental sensitive fracture of engineering materials: proceedings of symposium on environmental effects on fracture*. Metallurgical Society of AIME, Warrendale, PA, pp 326–360
- Birnbaum HK, Robertson IM, Sofronis P, Teter D (1997) Mechanisms of hydrogen related fracture—a review. In: Magnin T (ed) *Corrosion-deformation interactions*, CDF'96. The Institute of Materials, London, pp 172–195
- Birnbaum HK, Sofronis P (1994) Hydrogen-enhanced localized plasticity—a mechanism for hydrogen-related fracture. *Mater Sci Eng A* 176(1–2):191–202. doi:[10.1016/0921-5093\(94\)90975-X](https://doi.org/10.1016/0921-5093(94)90975-X)
- Cialone HJ, Holbrook JH (1988) Sensitivity of steels to degradation in gaseous hydrogen. In: Raymond L (ed) *Hydrogen embrittlement: prevention and control*, ASTM STP 962. ASTM, Philadelphia, PA, pp 134–152
- Choo WY, Lee JY (1982) Thermal analysis of trapped hydrogen in pure iron. *Metall Trans A* 13A:135–140
- Clark WAT, Wagoner RH, Shen ZY, Lee TC, Robertson IM, Birnbaum HK (1992) On the criteria for slip transmission across interfaces in polycrystals. *Scr Metall Mater* 26(2):203–206. doi:[10.1016/0956-716X\(92\)90173-C](https://doi.org/10.1016/0956-716X(92)90173-C)
- Dadfarnia M, Novak P, Ahn DC, Liu JB, Sofronis P, Johnson DD, Robertson IM (2010) Recent advances in the study of structural materials compatibility with hydrogen. *Adv Mater* 22(10):1128–1135. doi:[10.1002/adma.200904354](https://doi.org/10.1002/adma.200904354)
- Dadfarnia M, Martin ML, Nagao A, Sofronis P, Robertson IM (2015) Modeling hydrogen transport by dislocations. *J Mech Phys Solids* 78:511–525. doi:[10.1016/j.jmps.2015.03.002](https://doi.org/10.1016/j.jmps.2015.03.002)
- Ebihara K, Suzudo T, Kaburaki H, Takai K, Takebayashi S (2007) Modeling of hydrogen thermal desorption profile of pure iron and eutectoid steel. *ISIJ Int* 47:1131–1140. doi:[10.2355/isijinternational.47.1131](https://doi.org/10.2355/isijinternational.47.1131)
- Ebihara K, Kaburaki H, Suzudo T, Takai K (2009) A numerical study on the validity of the local equilibrium hypothesis in modeling hydrogen thermal desorption spectra. *ISIJ Int* 49:1907–1913. doi:[10.2355/isijinternational.49.1907](https://doi.org/10.2355/isijinternational.49.1907)
- Flanagan TB, Mason NB, Birnbaum HK (1981) The effect of stress on hydride precipitation. *Scripta Metall* 15(1):109–112. doi:[10.1016/0036-9748\(81\)90148-4](https://doi.org/10.1016/0036-9748(81)90148-4)
- Gangloff RP, Somerday BP (eds) (2012) *Gaseous hydrogen embrittlement of materials in energy technologies*. Woodhead Publishing, Cambridge
- Geng WT, Freeman AJ, Wu R, Geller CB, Reynolds JE (1999) Embrittling and strengthening effects of hydrogen, boron, and phosphorus on a $\Sigma 5$ nickel grain boundary. *Phys Rev B* 60(10):7149–7155. doi:[10.1103/PhysRevB.60.7149](https://doi.org/10.1103/PhysRevB.60.7149)
- Gerberich WW (2012) Modeling hydrogen induced damage mechanisms in metals. In: Gangloff RP, Somerday BP (eds) *Gaseous hydrogen embrittlement of materials in energy technologies*. Woodhead Publishing, Cambridge, pp 209–246
- Gerberich WW, Marsh PG, Hoehn JW (1996) Hydrogen induced cracking mechanisms—are there critical experiments? In: Thompson AW, Moody NR (eds) *Hydrogen effects in materials*. TMS, Warrendale, PA, pp 539–551
- Hirth JP (1984) Theories of hydrogen induced cracking of steels. In: Gibala R, Hehemann RF (eds) *Hydrogen embrittlement and stress corrosion cracking*. American Society for Metals, Metal Park, pp 29–41
- Hirth JP (1980) Effects of hydrogen on the properties of iron and steel. *Metall Trans A* 11(6):861–890. doi:[10.1007/BF02654700](https://doi.org/10.1007/BF02654700)
- Hirth JP, Rice JR (1980) On the thermodynamics of adsorption at interfaces as it influences decohesion. *Metall Trans A* 11(9):1501–1511. doi:[10.1007/BF02654514](https://doi.org/10.1007/BF02654514)
- Holbrook JH, Cialone HJ, Collings EW, Drauglis EJ, Scott PM, Mayfield ME (2012) Control of hydrogen embrittlement of metals by chemical inhibitors and coatings. In: Gangloff RP, Somerday BP (eds) *Gaseous hydrogen embrittlement of materials in energy technologies*. Woodhead Publishing, Cambridge, pp 129–153
- Hughes DA, Hansen N (2003) Deformation structures developing on fine scales. *Philos Mag* 83(31–34):3871–3893. doi:[10.1080/14786430310001605560](https://doi.org/10.1080/14786430310001605560)
- Johnson WH (1874) On some remarkable changes produced in iron and steel by the action of hydrogen and acids. *Proc R Soc Lond* 23:168–179. doi:[10.1098/rspl.1874.0024](https://doi.org/10.1098/rspl.1874.0024)
- Jokl ML, Vitek V, McMahon CJ Jr (1980) A microscopic theory of brittle fracture in deformable solids: a relation between ideal work to fracture and plastic work. *Acta Metall* 28(11):1479–1488. doi:[10.1016/0001-6160\(80\)90048-6](https://doi.org/10.1016/0001-6160(80)90048-6)
- Jones RH (1990) Analysis of hydrogen-induced subcritical intergranular crack growth of iron and nickel. *Acta Metall* 38(9):1703–1718. doi:[10.1016/0956-7151\(90\)90013-7](https://doi.org/10.1016/0956-7151(90)90013-7)
- Keller C, Hug E, Retoux R, Feaugas X (2010) TEM study of dislocation patterns in near-surface and core regions of deformed nickel polycrystals with few grains across the cross section. *Mech Mater* 42(1):44–54. doi:[10.1016/j.mechmat.2009.09.002](https://doi.org/10.1016/j.mechmat.2009.09.002)
- Kirchheim R (2007) Reducing grain boundary, dislocation line and vacancy formation energies by solute segregation. I. Theoretical background. *Acta Mater* 55(15):5129–5138. doi:[10.1016/j.actamat.2007.05.047](https://doi.org/10.1016/j.actamat.2007.05.047)
- Kirchheim R (2014) Diffusion controlled thermal desorption spectroscopy (TDS). In: *Steely hydrogen conference, proceedings*, Ghent, Belgium, pp e01/237–e01/254
- Kissinger HE (1957) Reaction kinetics in differential thermal analysis. *Anal Chem* 29(11):1702–1706
- Lassila DH, Birnbaum HK (1986) The effect of diffusive hydrogen segregation on fracture of polycrystalline nickel. *Acta Metall* 34(7):1237–1243. doi:[10.1016/0001-6160\(86\)90010-6](https://doi.org/10.1016/0001-6160(86)90010-6)
- Lee TC, Robertson IM, Birnbaum HK (1990a) In situ transmission electron microscope deformation study of the slip trans-

- fer mechanisms in metals. *Metall Trans A* 21(9):2437–2447. doi:[10.1007/BF02646988](https://doi.org/10.1007/BF02646988)
- Lee TC, Robertson IM, Birnbaum HK (1990b) TEM in situ deformation study of the interaction of lattice dislocations with grain boundaries in metals. *Philos Mag A* 62(1):131–153. doi:[10.1080/01418619008244340](https://doi.org/10.1080/01418619008244340)
- Li D, Gangloff RP, Scully JR (2004) Hydrogen trap states in ultrahigh-strength AERMET 100 steel. *Metall Mater Trans A* 35A:849–864
- Lynch S (2011) Hydrogen embrittlement (HE) phenomena and mechanisms. In: Raja VS, Shoji T (eds) *Stress corrosion cracking: theory and practice*. Woodhead Publishing, Cambridge, pp 90–130
- Martin ML, Fenske JA, Liu GS, Sofronis P, Robertson IM (2011a) On the formation and nature of quasi-cleavage fracture surfaces in hydrogen embrittled steels. *Acta Mater* 59(4):1601–1606. doi:[10.1016/j.actamat.2010.11.024](https://doi.org/10.1016/j.actamat.2010.11.024)
- Martin ML, Robertson IM, Sofronis P (2011) Interpreting hydrogen-induced fracture surfaces in terms of deformation processes: a new approach. *Acta Mater* 59(9):3680–3687. doi:[10.1016/j.actamat.2011.03.002](https://doi.org/10.1016/j.actamat.2011.03.002)
- Martin ML, Sofronis P, Robertson IM, Awane T, Murakami Y (2013) A microstructural based understanding of hydrogen-enhanced fatigue of stainless steels. *Int J Fatigue* 57:28–36. doi:[10.1016/j.ijfatigue.2012.08.009](https://doi.org/10.1016/j.ijfatigue.2012.08.009)
- Martin ML, Somerday BP, Ritchie RO, Sofronis P, Robertson IM (2012) Hydrogen-induced intergranular failure in nickel revisited. *Acta Mater* 60(6–7):2739–2745. doi:[10.1016/j.actamat.2012.01.040](https://doi.org/10.1016/j.actamat.2012.01.040)
- McNabb A, Foster PK (1963) A new analysis of the diffusion of hydrogen in iron and ferritic steels. *Trans Metall Soc AIME* 227:618–627
- Moody NR, Robinson SL, Garrison WMJ (1990) Hydrogen effects on the properties and fracture modes of iron-based alloys. *Res Mech* 30(2):143–206
- Munroe PR (2009) The application of focused ion beam microscopy in the material sciences. *Mater Charact* 60(1):2–13. doi:[10.1016/j.matchar.2008.11.014](https://doi.org/10.1016/j.matchar.2008.11.014)
- Murakami Y, Kanazaki T, Mine Y (2010) Hydrogen effect against hydrogen embrittlement. *Metall Mat Trans A* 41(10):2548–2562. doi:[10.1007/s11661-010-0275-6](https://doi.org/10.1007/s11661-010-0275-6)
- Nagao A, Dadfarnia M, Robertson IM, Sofronis P (2015) Hydrogen embrittlement mechanisms. In: Totten GE, Colas R (eds) *Encyclopedia of iron, steel, and their alloys*. Taylor & Francis Group, New York, NY In Press
- Nagao A, Martin ML, Dadfarnia M, Sofronis P, Robertson IM (2014) The effect of nano-sized (Ti, Mo)C precipitates on hydrogen embrittlement of tempered lath martensitic steel. *Acta Mater* 74:244–254. doi:[10.1016/j.actamat.2014.04.051](https://doi.org/10.1016/j.actamat.2014.04.051)
- Nagao A, Smith CD, Dadfarnia M, Sofronis P, Robertson IM (2014) Interpretation of hydrogen-induced fracture surface morphologies for lath martensitic steel. *Procedia Mater Sci* 3:1700–1705. doi:[10.1016/j.mspro.2014.06.274](https://doi.org/10.1016/j.mspro.2014.06.274)
- Nagao A, Smith CD, Dadfarnia M, Sofronis P, Robertson IM (2012) The role of hydrogen in hydrogen embrittlement fracture of lath martensitic steel. *Acta Mater* 60(13–14):5182–5189. doi:[10.1016/j.actamat.2012.06.040](https://doi.org/10.1016/j.actamat.2012.06.040)
- Novak P, Yuan R, Somerday BP, Sofronis P, Ritchie RO (2010) A statistical, physical-based, micro-mechanical model of hydrogen-induced intergranular fracture in steel. *J Mech Phys Solids* 58(2):206–226. doi:[10.1016/j.jmps.2009.10.005](https://doi.org/10.1016/j.jmps.2009.10.005)
- Ono K, Meshii M (1992) Hydrogen detrapping from grain boundaries and dislocations in high purity iron. *Acta Metall Mater* 40(6):1357–1364. doi:[10.1016/0956-7151\(92\)90436-I](https://doi.org/10.1016/0956-7151(92)90436-I)
- Oriani RA (1970) The diffusion and trapping of hydrogen in steel. *Acta Metall* 18(1):147–157. doi:[10.1016/0001-6160\(70\)90078-7](https://doi.org/10.1016/0001-6160(70)90078-7)
- Oriani RA, Josephic PH (1977) Equilibrium and kinetic studies of the hydrogen-assisted cracking of steel. *Acta Metall* 25(9):979–988. doi:[10.1016/0001-6160\(77\)90126-2](https://doi.org/10.1016/0001-6160(77)90126-2)
- Rice JR, Wang J (1989) Embrittlement of interfaces by solute segregation. *Mater Sci Eng A* 107(1–2):23–40. doi:[10.1016/0921-5093\(89\)90372-9](https://doi.org/10.1016/0921-5093(89)90372-9)
- Robertson IM (2001) The effect of hydrogen on dislocation dynamics. *Eng Fract Mech* 68(6):671–692. doi:[10.1016/S0013-7944\(01\)00011-X](https://doi.org/10.1016/S0013-7944(01)00011-X)
- Robertson IM, Birnbaum HK, Sofronis P (2009) Hydrogen effects on plasticity. In: Hirth JP, Kubin L (eds) *Dislocations in solids*. Elsevier, Oxford, pp 249–293
- Robertson IM, Sofronis P, Nagao A, Martin ML, Wang S, Gross DW, Nygren KE (2015) Hydrogen embrittlement understood. *Metall Mat Trans A* 46(6):2323–2341. doi:[10.1007/s11661-015-2836-1](https://doi.org/10.1007/s11661-015-2836-1)
- San Marchi C, Somerday BP (2012) Technical reference for hydrogen compatibility of materials. SAND2012-7321, Sandia National Laboratories, Livermore, CA
- Shih DS, Robertson IM, Birnbaum HK (1988) Hydrogen embrittlement of α titanium: in situ TEM studies. *Acta Metall* 36(1):111–124. doi:[10.1016/0001-6160\(88\)90032-6](https://doi.org/10.1016/0001-6160(88)90032-6)
- Shin KS, Meshii M (1983) Effect of sulfur segregation and hydrogen charging on intergranular fracture of iron. *Acta Metall* 31(10):1559–1566. doi:[10.1016/0001-6160\(83\)90153-0](https://doi.org/10.1016/0001-6160(83)90153-0)
- Smith E (1966) The nucleation and growth of cleavage microcracks in mild steel. In: Stickland AC (ed) *Proceedings of conference on physical basis of yield and fracture*. Institute of Physics and Physics Society, Oxford, pp 36–46
- Sofronis P, Birnbaum HK (1995) Mechanics of the hydrogen-dislocation-impurity interactions—I. Increasing shear modulus. *J Mech Phys Solids* 43(1):49–90. doi:[10.1016/0022-5096\(94\)00056-B](https://doi.org/10.1016/0022-5096(94)00056-B)
- Somerday BP, Sofronis P (eds) (2014) 2012 international hydrogen conference: hydrogen-materials interactions. ASME Press, New York, NY
- Somerday BP, Sofronis P, Nibur KA, San Marchi C, Kirchheim R (2013) Elucidating the variables affecting accelerated fatigue crack growth of steels in hydrogen gas with low oxygen concentrations. *Acta Mater* 61(16):6153–6170. doi:[10.1016/j.actamat.2013.07.001](https://doi.org/10.1016/j.actamat.2013.07.001)
- Staykov A, Yamabe J, Somerday BP (2014) Effect of hydrogen gas impurities on the hydrogen dissociation on iron surface. *Int J Quantum Chem* 114(10):626–635. doi:[10.1002/qua.24633](https://doi.org/10.1002/qua.24633)
- Stull DR, Prophet H (1971) JANAF thermochemical tables. 2nd edn. National Standard Reference Data System
- Suresh S, Ritchie RO (1982) Mechanistic dissimilarities between environmentally influenced fatigue-crack propagation at near-threshold and higher growth rates in lower strength steels. *Metal Sci* 16(11):529–538. doi:[10.1179/msc.1982.16.11.529](https://doi.org/10.1179/msc.1982.16.11.529)

- Suzuki H, Takai K (2012) Summary of round-robin tests for standardizing hydrogen analysis procedures. *ISIJ Int* 52:174–180. doi:[10.2355/isijinternational.52.174](https://doi.org/10.2355/isijinternational.52.174)
- Takai K (2011) Hydrogen existing states and hydrogen embrittlement. *Correl Eng* 60(5):230–235. doi:[10.3323/jcorr.60.230](https://doi.org/10.3323/jcorr.60.230)
- Takano S, Suzuki T (1974) An electron-optical study of β -hydride and hydrogen embrittlement of vanadium. *Acta Metall* 22(3):265–274. doi:[10.1016/0001-6160\(74\)90166-7](https://doi.org/10.1016/0001-6160(74)90166-7)
- Thompson AW, Bernstein IM (1980) Metallurgical variables in environmental fracture. In: Fontana MG, Staehle R (eds) *Advances in corrosion science and technology*. Plenum Publishing, New York, pp 53–175
- Yamaguchi T, Nagumo M (2003) Simulation of hydrogen thermal desorption under reversible trapping by lattice defects. *ISIJ Int* 43:514–519
- Wang S, Martin ML, Robertson IM, Sofronis P (2015) Effect of hydrogen environment on the separation of Fe grain boundaries. *Acta Mater* (under review)
- Wang S, Martin ML, Sofronis P, Ohnuki S, Hashimoto N, Robertson IM (2014) Hydrogen-induced intergranular failure of iron. *Acta Mater* 69:275–282. doi:[10.1016/j.actamat.2014.01.060](https://doi.org/10.1016/j.actamat.2014.01.060)
- Wei F-G, Enomoto M, Tsuzaki K (2012) Applicability of the Kissinger's formula and comparison with the McNabb–Foster model in simulation of thermal desorption spectrum. *Comput Mater Sci* 51:322–330. doi:[10.1016/j.commatsci.2011.07.009](https://doi.org/10.1016/j.commatsci.2011.07.009)
- Wei FG, Tsuzaki K (2006) Quantitative analysis on hydrogen trapping of TiC particles in steel. *Metall Mater Trans A* 37A:331–353. doi:[10.1007/s11661-006-0004-3](https://doi.org/10.1007/s11661-006-0004-3)
- Wu R, Freeman AJ, Olson GB (1994) First principles determination of the effects of phosphorus and boron on iron grain boundary cohesion. *Science* 265(5170):376–380. doi:[10.1126/science.265.5170.376](https://doi.org/10.1126/science.265.5170.376)
- Yamaguchi T, Nagumo M (2003) Simulation of hydrogen thermal desorption under reversible trapping by lattice defects. *ISIJ Int* 43:514–519. doi:[10.2355/isijinternational.43.514](https://doi.org/10.2355/isijinternational.43.514)
- Zhong L, Wu R, Freeman AJ, Olson GB (2000) Charge transfer mechanism of hydrogen-induced intergranular embrittlement of iron. *Phys Rev B* 62(21):13938–13941. doi:[10.1103/PhysRevB.62.13938](https://doi.org/10.1103/PhysRevB.62.13938)